Kobe University Repository : Kernel

PDF issue: 2026-07-15

Zero-Phase-Angle Load-Independent and -Adaptable Dual-Side LCC Inductive Wireless Power Transfer System

Mishima, Tomokazu

Lai, Ching-Ming

(Citation)
IEEE Transactions on Transportation Electrification,10(2):3492-3503

(Issue Date)
2023-08-17

(Resource Type)
journal article

(Version)
Accepted Manuscript

(Rights)
© 2023 IEEE. Personal use of this material is permitted. Permission from IEEE must be obtained for all other uses, in any current or future media, including reprinting/republishing this material for advertising or promotional purposes, creating new collective works, for resale or redistribution to servers or lists, or…

(URL)
https://hdl.handle.net/20.500.14094/0100490460

This article has been accepted for publication in IEEE Transactions on Transportation Electrification. This is the author's version which has not been fully edited and content may change prior to final publication. Citation information: DOI 10.1109/TTE.2023.3305057

Zero-Phase-Angle Load-Independent and -Adaptable Dual-Side LCC Inductive Wireless Power Transfer System

Tomokazu Mishima, *Senior Member, IEEE,* and Ching-Ming Lai, *Senior Member, IEEE*

***Abstract*—This paper presents a zero phase angle (ZPA) load-independent and -adaptable (LIA) high-order resonant inductive wireless power transfer (IPT) systems. By designing a ZPA frequency that makes all the mesh networks resonate at the same frequency, constant current (CC) or constant voltage (CV) output mode is achievable for the load variations with voltage / current source. In addition to the frequency-domain analysis, characteristics of the high-order IPT are investigated by a dual-side LCC (D-LCC) resonant tanks, where the load power can be controlled over the wide range by pulse frequency modulation (PFM) / phase shift pulse width modulation (PS-PWM) hybrid controller. The PS-PWM and PFM hybrid modulation overcomes the issues of the existing power controls for load independent WPT. The performances of the proposed IPT system are evaluated by experiment of 5 kW prototype, after which the validity of the system design methodology is evaluated from the practical points of view.**

***Index Terms*—Dual-side LCC (D-LCC), high order resonant tank, inductive wireless power transfer (IPT), load-independent, zero-phase-angle (ZPA), zero voltage soft switching (ZVS).**

NOMENCLATURE

L_1	Self inductance of transmitter (Tx) coil
L_2	Self inductance of receiver (Rx) coil
L_{s1}	Series inductor in Tx side
L_{s2}	Series inductor in Rx side
L_{k1}	Leakage inductance of Tx coil
L_{k2}	Leakage inductance of Rx coil
C_{p1}	Parallel capacitor in Tx side
C_{p2}	Parallel capacitor in Rx side
C_{s1}	Series capacitor in Tx side
C_{s2}	Series capacitor in Rx side
k	Coupling coefficient between Tx and Rx coils
M	Mutual inductance between Tx and Rx coils
R_1	Resistance of Tx coil
R_2	Resistance of Rx coil
R_M	Equivalent resistance in the mutual inductance
Z_{in}	Driving point impedance
Z_T	Impedance in Thévenin equivalent circuit
V_T	Voltage source in Thévenin equivalent circuit
v_{ac}	Ac voltage source in equivalent circuit
$\dot{V}_o$	Voltage vector of ac output
R_o	Dc load resistance
R_o^*	Rated dc load resistance
R_{eq}	Equivalent ac load resistance
f_s	Switching frequency.
f_r	ZPA frequency of Z_{in}
f_o	Switching frequency at maximum power
ω_s	Angular switching frequency
ω_r	Angular ZPA frequency
λ	Load impedance ratio (R_o/R_o^*)
ϕ	Phase shift (PS) angle
ζ	Dc voltage conversion ratio
V_{in}	Input dc voltage
P_o	Output power
P_o^*	Output power rating
V_o	Output dc voltage
I_o	Output dc current
I_{omax}	Dc current rating
$I_{o,\phi}$	Output dc current with PS angle.

T. Mishima is with the Div. of Marine Technologies and Engineering, Faculty of Oceanology and Graduate School of Maritime Sciences, Kobe University, Hyogo, Japan (e-mail: mishima@maritime.kobe-u.ac.jp).

C.-M. Lai, the corresponding author, is with the Department of Electrical Engineering, National Chung Hsing University, Taichung, Taiwan (e-mail: pecmlai@gmail.com).

This paper is the improved and expanded version of the conference proceedings in IEEE Applied Power Electronics and Expositions (IEEE-APEC) 2021, New Orleans, Louisiana/Virtual.

This research is supported by 2022 Kobe University Strategic International Collaborative Research Grant. This paper is the improved and expanded version of the conference proceedings in IEEE Applied Power Electronics and Expositions (IEEE-APEC) 2021, New Orleans, Louisiana/Virtual.

I. INTRODUCTION

THE inductive wireless power transfer (IPT) systems are drawing much attentions as a key technology for pushing forward electrifications in automobiles, vehicles, railway, ships [1] [2]. The resonant tanks are essential items in compensating weak magnetic flux-linkage between transmitting (Tx) and receiving (Rx) coils, and significantly relevant for performances of IPT system in terms of power capacity, short- / open-load protection, output power regulations, and system robustness [3]- [6] as illustrated in Fig. 1. In particular, high-order resonant tanks such as dual-side LCC (D-LCC) naturally have load independence of zero–phase-angle (ZPA) in the driving point impedance, which leads to a wide range of soft switching and high power factor of the high-frequency inverter [7], [8].

Design methods for load-independent constant current (CC) or constant voltage (CV) output are mentioned in the past literatures such as in [9]- [12]. The reverse-/normal-L, T- and Π-circuits are adopted in [9] to constitute the multi-resonant tanks and achieve the load-independent CC/ CV output modes. However, the ZPA condition is not deeply discussed therein,

Authorized licensed use limited to: National Chung Hsing Univ.. Downloaded on August 18,2023 at 12:15:43 UTC from IEEE Xplore. Restrictions apply.
© 2023 IEEE. Personal use is permitted, but republication/redistribution requires IEEE permission. See https://www.ieee.org/publications/rights/index.html for more information.

This article has been accepted for publication in IEEE Transactions on Transportation Electrification. This is the author's version which has not been fully edited and content may change prior to final publication. Citation information: DOI 10.1109/TTE.2023.3305057

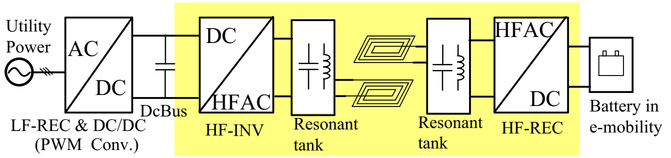

Fig. 1. Power conversion process in IPT system for EVs battery charger (the colored area is the target of research).

and the switching frequencies are set outside the frequency range (81.38 kHz-90 kHz) claimed by SAE (Society of Automotive Engineers) [13]. The similar concept of ZPA load-independence featuring CC/CV design method is presented by setting two ZPA frequencies in [10] and [11]. The load-independent CC and CV output modes are achievable by exchanging the two ZPA frequencies alternately in accordance with the load conditions. However, a design method in [10] are limited for the operating conditions of fixed current and voltage in CC and CV output modes. Furthermore, the circuit parameters significantly depend on the coupling co-efficient and mutual inductance in Tx and Rx coils as revealed in [11], thus it is hard to decide the two ZPA frequencies within the SAE standard as aforementioned. A unified theory of high-order resonant tank is explained in [12], and a method of changing the mesh numbers to attain the load-independence in both CC and CV output modes. The theory exhibits a design method for considering the ZPA and load-independent output simultaneously, however it is incomplete due to the limited discussions; i) the current-source input is not adaptable, ii) the parameter design process in the actual system is not revealed, and iii) the load adaptability cannot be ensured for the variable commands of output current and voltage.

The misalignment-tolerant D-LCC IPT system is proposed in [14], by featuring load-independent (LI)-CC and CV outputs. The technical concern exists in a large circulating current of the resonant tanks which causes efficiency deterioration. The reconfigurable D-LCC IPT system is proposed in [15] by featuring high power factor with switched capacitors, however the cost-effectiveness might be lost. The semibridgeless active rectifier-based D-LCC resonant converter is proposed for IPT systems in [16]. The constant-frequency pulse modulation is achievable, however high frequency ringing may arise at the turn-off transition of the active switches in the semibridgless active rectifier, whereby electromagnetic noise emission inherently becomes outstanding [17]. The asymmetrical tuned D-LCC IPT is presented in [18] featuring an efficiency optimization. However the power rating significantly depends on the self inductances of Tx and Rx coils in the asymmetrically tuned D-LCC resonant tanks, which leads to limitation of system specifications. The high power (20 kW) D-LCC IPT featuring bidirectional power flow is proposed in [19], however the load independent CC and CV modes are discussed in details.

On the whole, no power control scheme effective both for load independence in ZVS and adaptability to command variations in CC and CV has been established in the existing technologies. In order to overcome the technical constraints, this paper presents a ZPA load-independent and -adaptable (LIA) IPT system with D-LCC resonant tank suitable for power control of CC and CV output modes in the battery charging applications. By creating all the mesh networks resonate with an identical frequency based on T-type circuit models, the load current or voltage can be regulated naturally as CC or CV mode with ZPA. Although ZPA-load independence is ensured solely in CC mode, it can be attained for CV mode by adopting pulse frequency modulation (PFM) and phase shift pulse width modulation (PS-PWM). The current and voltage commands of CC and CV modes can also be regulated by the hybrid pulse modulations, thereby adaptability for the command value variations can be ensured.

The rest of this paper is organized as follows: the power circuit and controller configuration of the proposed ZPA-LIA IPT system are described in Section II. The principle of ZPA-CC mode with the voltage source inverter is also explained with referring to Appendix. The pulse modulations for the Tx-side high frequency inverter and the power control principle are revealed for CC and CV modes respectively in Section III. The performances of the proposed IPT system are demonstrated by simulation and experiment in Section IV, then the feasibility is evaluated in details. Finally, the characteristics of the proposed IPT are summarized in Section V from the practical point of view.

II. ZPA-LIA IPT SYSTEM

The circuit and system diagram of a D-LCC-based ZPA-LIA IPT system is displayed in Fig. 2 [20]. This system incorporates a closed-loop control mechanism, which effectively addresses the challenges posed by system parameter drifts through automatic frequency-tuning. The primary-side power stage is a high frequency three-level inverter (HFTL-INV) which consists of a flying capacitor and clamping diode, aiming for reduction of voltage stress in power devices with PS-PWM. The neutral clamping diodes $\mathrm{D_{c1}}$ and $\mathrm{D_{c2}}$ provide the surge voltage protection; thus the hard switching is mitigated especially in $\mathrm{Q_1}$ and $\mathrm{Q_4}$. The flying capacitor C_{fy} is dedicated for PS-PWM intervals between $\mathrm{Q_1}$ and $\mathrm{Q_4}$ as well as $\mathrm{Q_2}$ and $\mathrm{Q_3}$ [21]. The parasitic output capacitances C_{s1}-C_{s4} help to reduce dv/dt rate at the turn-off transitions of $\mathrm{Q_1}$-$\mathrm{Q_4}$ for ZVS. Note here that this IPT is not limited for three-level HF-INV but a full-bridge topology is also applicable in principle.

Fig. 3 reveals the key waveforms of the ZPA-LIA IPT system with a PS angle ϕ. The circuit-state transitions of a switching cycle during t_1-t_{12} are divided into the twelve modes. The detailed descriptions of the mode transitions are same as presented in [20], which are excluded herein for the sake of page limit. The commutations of the active switches $\mathrm{Q_1}$–$\mathrm{Q_4}$ depend significantly on the pulse modulations. When PFM is applied for $\mathrm{Q_1}$–$\mathrm{Q_4}$ where the two-level rectangular waveform appears in v_{ab} with high load-power factor, the switching waveforms are identical in $\mathrm{Q_1}$–$\mathrm{Q_4}$; ZVS turn-on transition can be ensured while near zero current-assisted ZVS turn-off transition can attain in each switch. When PS-PWM is adopted in the HFTL-INV, the fixed switches $\mathrm{Q_1}$ and $\mathrm{Q_4}$ are commutated by ZVS at the turn-off transitions. Since the

Authorized licensed use limited to: National Chung Hsing Univ.. Downloaded on August 18,2023 at 12:15:43 UTC from IEEE Xplore. Restrictions apply.
© 2023 IEEE. Personal use is permitted, but republication/redistribution requires IEEE permission. See https://www.ieee.org/publications/rights/index.html for more information.

This article has been accepted for publication in IEEE Transactions on Transportation Electrification. This is the author's version which has not been fully edited and content may change prior to final publication. Citation information: DOI 10.1109/TTE.2023.3305057

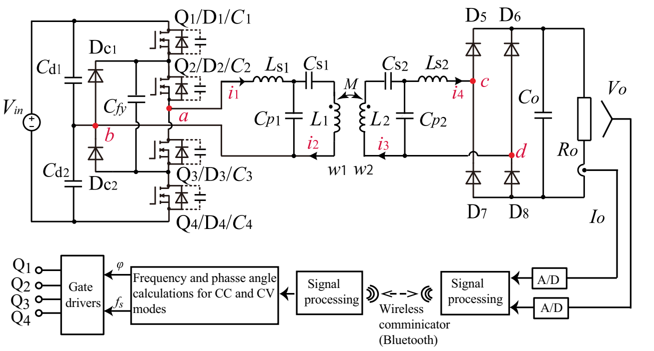

Fig. 2. Main circuit and control system of a ZPA-LIA IPT system based on D-LCC tanks.

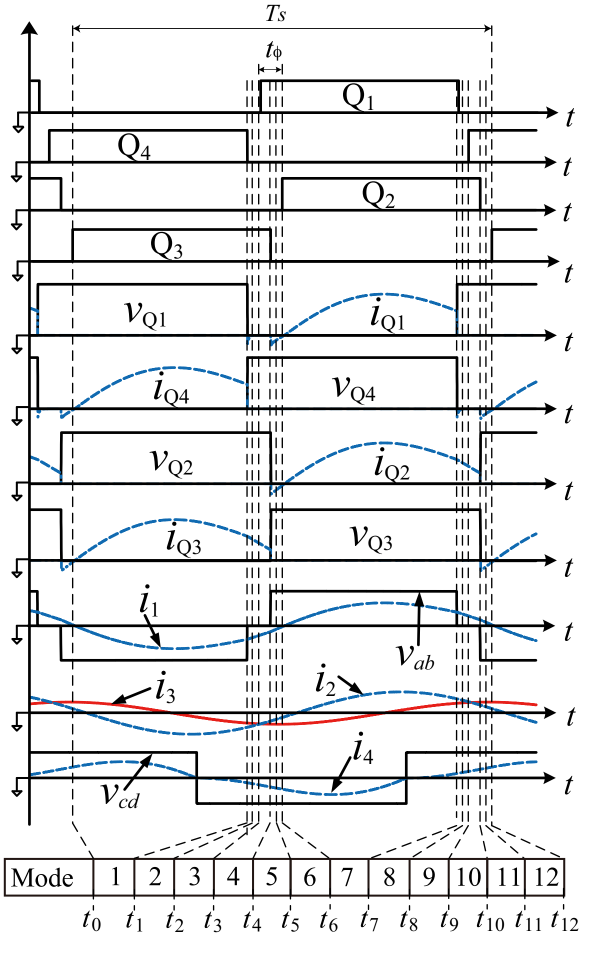

Fig. 3. Key waveforms for a switching cycle with PS-PWM ($t_\phi = (\phi/360°)\cdot T_s$).

current through the controlled-phase switches Q_2 and Q_3 is prone to leading-phase by PS-PWM, it is hard to keep soft commutations at both their turn-on and -off transitions in CC mode due to ZPA. However, this occurs only for CC mode with a command of load current smaller than the nominal value.

The equivalent circuit of the power stage is revealed in Fig. 4, where the resistances of the passive components including Tx and Rx coils are neglected for simplifying the analysis with respect to the operating frequency less than 100 kHz. When the fundamental harmonic approximation (FHA) is employed

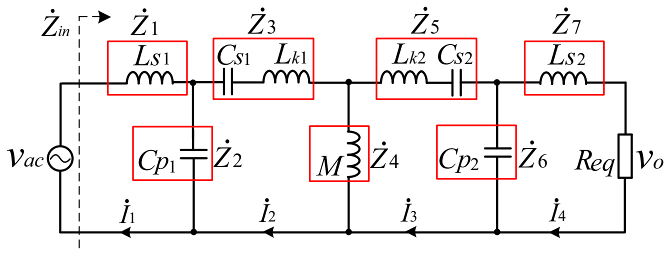

Fig. 4. Equivalent circuit based on the primary-side referred T-type model of Tx and Rx coils (a=1) (see in Appendix).

in Fig. 4, the ac source $v_{ac}(\dot{V}_{ac})$ denotes the fundamental component of inverter bridge-leg voltage v_{ab}, RMS value V_{ac} of which is expressed by where ϕ is limited within $0° \le \phi < 180°$.

$$\left.\begin{aligned} V_{ac} &= \frac{\sqrt{2}V_{in}}{\pi} \quad \text{(for PFM)} \\ &= \frac{(1+\cos\phi)V_{in}}{\sqrt{2}\pi} \quad \text{(for PS-PWM)} \end{aligned}\right\} \tag{1}$$

The Tx and Rx coils are divided into the three inductances; L_1, L_2 and M all of which are expressed by T-shape mode of Tx and Rx coils (see in Appendix). The ac equivalents resistance R_{eq} represents the full bridge diode rectifier and dc load, which can be given with the windings turns ratio $a = w_1/w_2$ and the dc load resistance R_o as

$$R_{eq} = \frac{8a^2 R_o}{\pi^2}. \tag{2}$$

The impedances in D-LCC should satisfy the conditions as (see in Appendix)

$$\begin{cases} j\omega_r L_{s1} + \dfrac{1}{j\omega_r C_{p1}} = 0 \\ \dfrac{1}{j\omega_r C_{p1}} + \dfrac{1}{j\omega_r C_{s1}} + j\omega_r(L_{k1}+M) = 0 \\ \dfrac{1}{j\omega_r C_{p2}} + \dfrac{1}{j\omega_r C_{s2}} + j\omega_r(L_{k2}+M) = 0 \\ j\omega_r L_{s2} + \dfrac{1}{j\omega_r C_{p2}} = 0. \end{cases} \tag{3}$$

Notice that $\omega_r (= 2\pi f_r)$ in (3) is the ZPA angular frequency for load independence in CC mode. The T-connection circuit model-based ZPA condition can be extended for higher-order resonant converters with intermediate coils for the wider gap scenario [22]. Considering the KVL in every mesh of Fig. 4, the ac current I_4 is decided at the switching frequency $f_s = f_r$ as

$$I_4 = \left|\frac{\dot{Z}_4}{\dot{Z}_2\dot{Z}_6}\right| V_{ac}. \tag{4}$$

The Bode diagrams of the driving-point impedance Z_{in}, the transconductance $G_{\mathrm{vi}} (= I_4/V_{ac})$ and the ac voltage ratio $G_{ac} (= Vo/V_{ac})$ are shown with load variations in Fig. 5 with a set of numerical example of circuit parameters. The ZPA angle emerges where G_{vi} is fixed regardless of the load as illustrated in the curves, which indicates the load-independent CC mode can attain under the condition of (3).

Authorized licensed use limited to: National Chung Hsing Univ.. Downloaded on August 18,2023 at 12:15:43 UTC from IEEE Xplore. Restrictions apply.
© 2023 IEEE. Personal use is permitted, but republication/redistribution requires IEEE permission. See https://www.ieee.org/publications/rights/index.html for more information.

This article has been accepted for publication in IEEE Transactions on Transportation Electrification. This is the author's version which has not been fully edited and content may change prior to final publication. Citation information: DOI 10.1109/TTE.2023.3305057

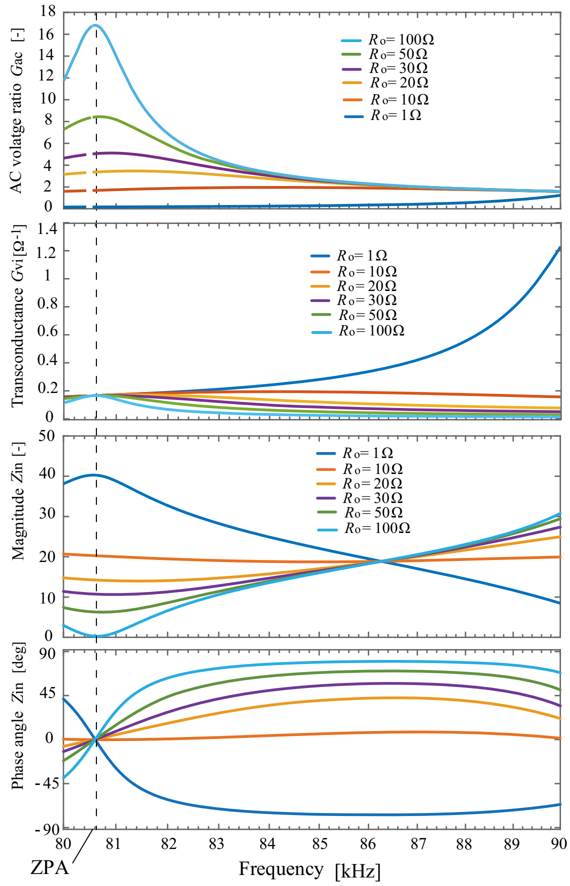

Fig. 5. Bode diagram of the driving point impedance Z_{in}, the transconductance G_{vi} and the voltage ration G_{ac} of the equivalent circuit ($a = 1$, $L_{s1} = L_{s2} = 23.5\,\mu$H, $C_{s1} = C_{s2} = 38.4\,$nF, $C_{p1} = C_{p2} = 166\,$nF, $L_1 = L_2 = 125\,\mu$H, $k = 0.22$).

III. Pulse Modulations and Power Control

The hybrid PFM / PS-PWM modulation is adopted in the ZPA-LIA IPT system to perform the CC and CV output modes. The concept of the hybrid pulse modulations is portrayed in Fig. 6 (a) with CC and CV mode profiles respectively.

A. Current Current (CC) Mode

The D-LCC IPT system can naturally maintain CC output mode, however the current command should be adjusted in accordance with the power rating as well as the coupling coefficient between Tx and Rx coils. PS-PWM is suitable for achieving the load current regulation since it does not change the fundamental frequency of the leg voltage v_{ab} in the HFTL-INV. The dc output current can be obtained by regulating ϕ from (4) as

$$\begin{aligned} I_{o,\phi} &= \left| \frac{\dot{Z}_4}{\dot{Z}_2 \dot{Z}_6} \right| \frac{2\sqrt{2}}{\pi} \frac{(1+\cos\phi)V_{in}}{\sqrt{2}\pi} \\ &= \omega_r^3 M C_{p1} C_{p2} \frac{2(1+\cos\phi)V_{in}}{\pi^2}. \end{aligned} \tag{5}$$

The control algorithm for the load current regulation is displayed by flow chart in Fig. 6(b). In addition, the gate-driving pulse patterns for CC mode are shown in Fig. 6(c)

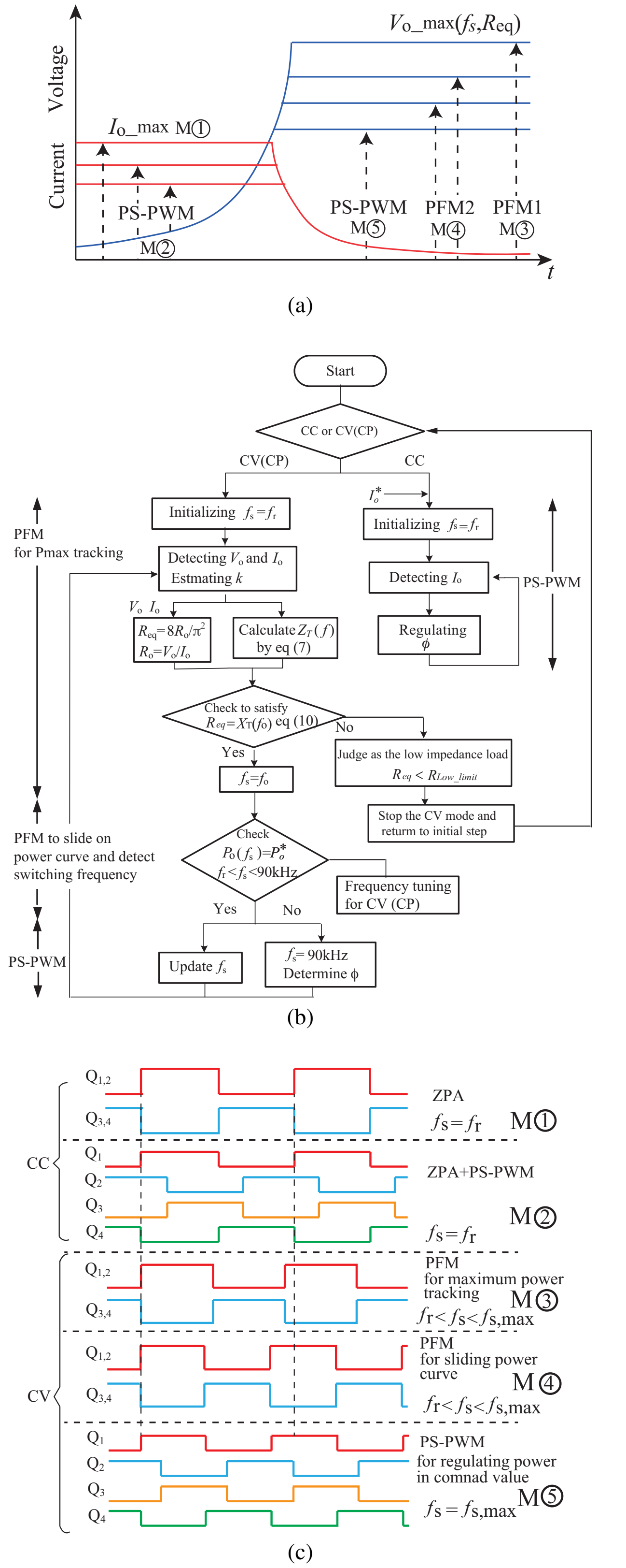

Fig. 6. Principle of PFM/PS-PWM hybrid power controls: (a) CCCV battery charger profile, (b) flow chart, and (c pulse patterns of modulations.

which corresponds to M1 and M2. The pulse frequency is fixed at the ZPA frequency, then the load current is regulated

Authorized licensed use limited to: National Chung Hsing Univ.. Downloaded on August 18,2023 at 12:15:43 UTC from IEEE Xplore. Restrictions apply.
© 2023 IEEE. Personal use is permitted, but republication/redistribution requires IEEE permission. See https://www.ieee.org/publications/rights/index.html for more information.

This article has been accepted for publication in IEEE Transactions on Transportation Electrification. This is the author's version which has not been fully edited and content may change prior to final publication. Citation information: DOI 10.1109/TTE.2023.3305057

$$\dot{V}_T = \frac{\dot{V}_{ac}}{C_{p2}\left[(\omega_s^4 L_{s1}C_{p1}-\omega_s^2)\left\{\frac{\left(L_{k1}+M-\frac{C_{p1}+C_{s1}}{\omega_s^2 C_{p1}C_{s1}}\right)\left(L_{k2}+M-\frac{C_{p2}+C_{s2}}{\omega_s^2 C_{p2}C_{s2}}\right)}{M}-M\right\}-\frac{L_{k2}+M-\frac{C_{p2}+C_{s2}}{\omega_s^2 C_{p2}C_{s2}}}{\omega_s M C_{p1}^2}\right]} \tag{6}$$

$$\dot{Z}_T = j\left[\omega_s L_{s2}-\frac{L_{k2}-\frac{1}{\omega_s^2 C_{s2}}+\frac{M\left(\omega_s^2 L_{k1}C_{s1}+\omega_s^2 L_{s1}C_{p1}+\omega_s^2 L_{s1}C_{s1}-\omega_s^2 L_{k1}L_{s1}C_{p1}C_{s1}-1/\omega_s^2\right)}{(L_{k1}C_{s1}+L_{c1}C_{p1}+L_{s1}C_{s1}+MC_{s1})-\omega_s^2 L_{s1}(L_{k1}+M)C_{p1}C_{s1}-1/\omega_s^2}}{\omega_s C_{p2}\left\{L_{k2}-\frac{C_{p2}+C_{s2}}{\omega_s^2 C_{p2}C_{s2}}+\frac{M(L_{k1}C_{s1}+L_{s1}C_{p1}+L_{s1}C_{s1}-\omega_s^2 L_{k1}L_{s1}C_{p1}C_{s1}-1/\omega_s^2)}{(L_{k1}C_{s1}+L_{s1}C_{p1}+L_{s1}C_{s1}+MC_{s1})-\omega_s^2 L_{s1}(L_{k1}+M)C_{p1}C_{s1}-1/\omega_s^2}\right\}}\right] \tag{7}$$

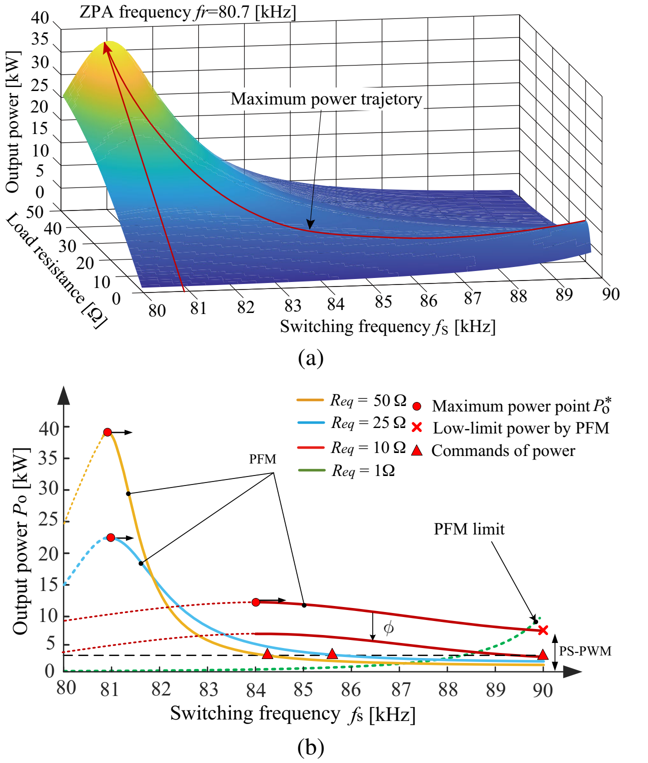

Fig. 7. Power curves with the PFM/PS-PWM hybrid control: (a) characteristics of $P_o - f_s - R_o$ and (b) transitions of operating points ($|v_{ac}| = 400$ V, $L_{c1} = L_{s2} = 23.5\,\mu$H, $C_{s1} = C_{s2} = 38.4$ nF, $C_{p1} = C_{p2} = 166$ nF, $L_1 = L_2 = 125\,\mu$H, $k = 0.22$).

by PS-PWM.

B. Constant Voltage (CV) Mode

The voltage source $\dot{V}_T$ and internal impedance $\dot{Z}_T = jX_T$ can be defined from Fig. 4 as (6) and (7) while $\omega_s (= 2\pi f_s)$ denotes an angular switching frequency. The load current $\dot{I}_4$ can be given by

$$\dot{I}_4 = \frac{\dot{V}_T}{(R_{eq}+jX_T)} = \frac{R_{eq}-jX_T}{R_{eq}^2+X_T^2}\dot{V}_T. \tag{8}$$

Accordingly, the output power P_o can be obtained as

$$P_o = R_{eq}\left|\frac{R_{eq}-jX_T}{R_{eq}^2+X_T^2}\cdot\dot{V}_T\right|^2. \tag{9}$$

By yielding the derivative dP_o/dR_{eq} to zero, the maximum power condition can be expressed as

$$R_{eq} = X_T(f_o). \tag{10}$$

where f_o denotes the switching frequency at the maximum load power P_o^*. The switching frequency f_s is regulated so that P_o corresponds with its command value P_o^* as long as f_s is less than its upper limit (90 kHz).

Fig. 7 (a) shows the output power characteristics with f_s and load resistance R_o. As a numerical example, the circuit parameters are designed for a 30 kW system and the resonant frequency is set around 81 kHz. While the ZPA frequency is fixed for CC mode with the load variations, the trajectory of maximum power is not linear at the resonant frequency. The transitions of the operating point are depicted in Fig. 7 (b). The operation area should exist in the switching frequency area higher than that of maximum power point in order to ensure the inductive $\dot{Z}_{in}$ for ZVS. PFM can accommodate the high load impedance with the frequency range between 81 kHz and 90 kHz, and P_o can be controlled. However, it is not controllable over the high-end frequency of 90 kHz under the condition of low load impedances, accordingly PS-PWM is activated for covering the rest part of power range.

The switching frequency should start from the value where (10) is satisfied and the maximum power is obtained so that the lagging-phase (inductive) current and ZVS are available in the HFTL-INV. Accordingly, PFM in M③ is the first stage of CV output mode, after which the load power is controlled by PFM within 81 kHz-90 kHz in M④. Since PFM is limited under the high-end 90 kHz, the pulse modulation changes to PS-PWM for power regulation in M⑤. It should be remarked here the HFTL-INV is disconnected from the power source V_{in} when (10) cannot be established due to low impedance of the dc load, i.e. overload condition.

The commutations of all the switches are summarized in TABLE I. The semi-ZVS denotes an incomplete soft switching due to residual voltages in the parasitic capacitances of the active switches [23]. The ZVS condition in Q_1–Q_4 with PS-PWM can be expressed in terms of phase angle of Z_{in} at $f_o < f_r < f_{s,max}$ as

$$\phi \leq 2\tan^{-1}\left\{\frac{\mathrm{Im}(\dot{Z}_{in})}{\mathrm{Re}(\dot{Z}_{in})}\right\}. \tag{11}$$

IV. Simulation and Experimental Verification

A. Simulation Analysis

The simulation results for the dynamics of load voltage regulations are displayed in Fig. 8. The dc-source voltage V_{in} is set as 800 V dc voltage source with power rating of 15 kW,

Authorized licensed use limited to: National Chung Hsing Univ.. Downloaded on August 18,2023 at 12:15:43 UTC from IEEE Xplore. Restrictions apply.
© 2023 IEEE. Personal use is permitted, but republication/redistribution requires IEEE permission. See https://www.ieee.org/publications/rights/index.html for more information.

This article has been accepted for publication in IEEE Transactions on Transportation Electrification. This is the author's version which has not been fully edited and content may change prior to final publication. Citation information: DOI 10.1109/TTE.2023.3305057

TABLE I
SWITCHING CONDITIONS WITH PULSE MODULATIONS

Pulse patters	Modulations	Q_1	Q_2	Q_3	Q_4	ZPA	Output
M①	Fixed frequency	Semi-ZVS	Semi-ZVS	Semi-ZVS	Semi-ZVS	◯	CC
M②	PS-PWM	ZVS	H-SW	H-SW	ZVS	◯	CC
M③	PFM	ZVS	ZVS	ZVS	ZVS	◯	CV
M④	PFM	ZVS	ZVS	ZVS	ZVS	◯	CV
M⑤	PS-PWM	ZVS	ZVS*	ZVS*	ZVS	△	CV

*Available only under the condition (11).

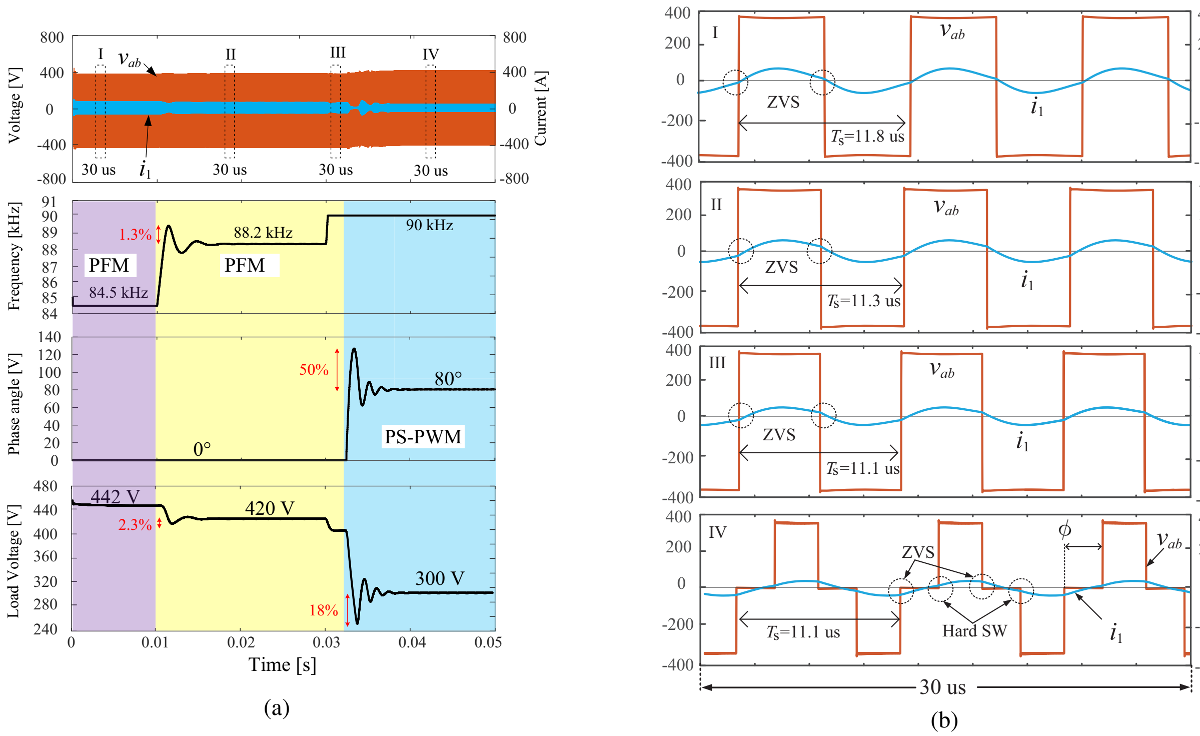

Fig. 8. Simulation waveforms for algorithm verification: (a) transitional operating waveforms, and (b) voltage and current in the HFTL-INV at $V_o^* = 420$V at $t = 0.01$s and $V_o^* = 300$V at $t = 0.03$s ($V_{in} = 800$V, $R_o = 12\Omega$, $L_{s1} = L_{s2} = 23.5\mu$H, $C_{s1} = C_{s2} = 38.4$nF, $C_{p1} = C_{p2} = 166$nF, $L_1 = L_2 = 125\mu$H, $k = 0.22$.)

and the reference value of V_o varies from $420\,\mathrm{V}$ to $300\,\mathrm{V}$ at $t = 0.03$s. In the first interval, PFM of M③ is activated for tracking the maximum power, thereby f_s is regulated at $84.5\,\mathrm{kHz}$ with $V_o = 442\,\mathrm{V}$. In the following interval, PFM (M④) is activated for regulating V_o to $420\,\mathrm{V}$, whereby f_s is controlled to $88.2\,\mathrm{kHz}$. When the voltage reference changes to $300\,\mathrm{V}$, PFM cannot be available since f_s reaches the upper limit $f_{s,max} = 90\,\mathrm{kHz}$. Then, PS-PWM (M⑤) starts to activate and complete the final step of voltage regulations. During the whole process, ZVS can attain in the HFTL-INV.

The voltage and current waveforms in the HFTL-INV are drawn in Fig. 8(b) at the scoped areas I-IV, respectively: PFM for the area I–III and PS-PWM for IV. It can be known hereby that high power factor operations can maintain in the proposed pulse modulation.

The performances for the Tx and Rx coils' misalignment are simulated under the scenario of X-Y misalignment ranging from 0 to $100\,\mathrm{mm}$ as drawn in Fig. 9. It is confirmed from Fig. 10 that the LI-ZPA can maintain for the variation of k. The dc-dc power conversion efficiencies are estimated by simulation under the conditions of X-Y misalignments in

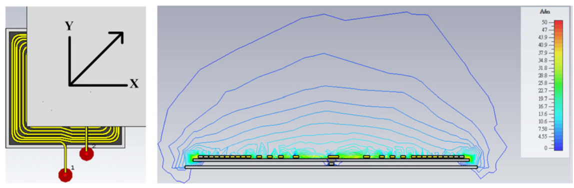

Fig. 9. X-Y misalignment scenarios of Tx/Rx coils and magnetic analysis.

Fig. 11. It can be predicted from the system efficiency will decrease due to the reductions in the coupling coefficient k while the relatively high efficiency can maintain in the range between 0 to $40\,\mathrm{mm}$ of X-Y misalignment.

B. Prototype Specification

The experiment verification of the proposed IPT system is carried out on the basis of a downsized prototype.

The exterior appearance of the experimental system is presented in Fig. 12. The specifications of all the circuit parameters in the prototype are listed in TABLE II. The

Authorized licensed use limited to: National Chung Hsing Univ.. Downloaded on August 18,2023 at 12:15:43 UTC from IEEE Xplore. Restrictions apply.
© 2023 IEEE. Personal use is permitted, but republication/redistribution requires IEEE permission. See https://www.ieee.org/publications/rights/index.html for more information.

This article has been accepted for publication in IEEE Transactions on Transportation Electrification. This is the author's version which has not been fully edited and content may change prior to final publication. Citation information: DOI 10.1109/TTE.2023.3305057

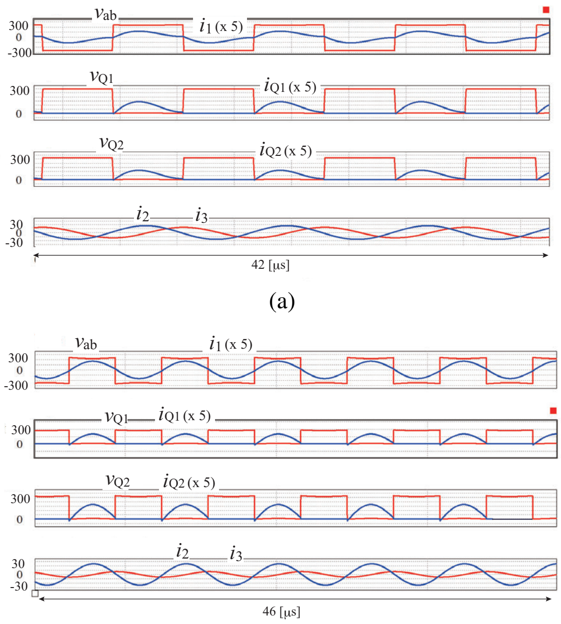

(a)

(b)

Fig. 10. Simulation waveforms for the variations of coupling coefficient due to misalignment: (a) $X = 100\,\mathrm{mm}$, $Y = 100\,\mathrm{mm}$, and $k = 0.13$, and (b) $X = 0\,\mathrm{mm}$, $Y = 0\,\mathrm{mm}$, and $k = 0.22$.

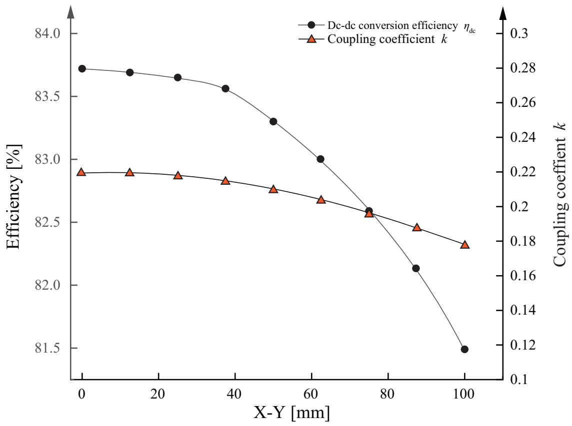

Fig. 11. Estimated system efficiency under the condition of X-Y misalignment.

wide-band-gap semiconductor Silicon Carbide (SiC) power MOSFETs (IXFN50N120SK, $1200\,\mathrm{V}$, $48\,\mathrm{A}$, $50\,\mathrm{m\Omega}$) and fast recovery diode (DESI2X101-06A, $1000\,\mathrm{V}$, $200\,\mathrm{A}$, $0.7\,\mathrm{V}$) are employed for the HFTL-INV in order to ensure the fast switching transitions, low on-resistance and excellent thermal cooling.

The windings structures of rectangular (square) Tx and Rx coils are shown in Fig. 13 (a) and (b). The rectangular coils with high frequency Litz wires are more unsusceptible to the misalignment than circular and rectangular ones, which is beneficial for transportation IPT systems. The relevant circuit parameters are listed in TABLE III.

The dc input voltage is set as $V_{in} = 250\,\mathrm{V}$ and the power rating is designed as $5\,\mathrm{kW}$ at $R_o^* = 48\,\Omega$ $(100\,\%)$ for the sake

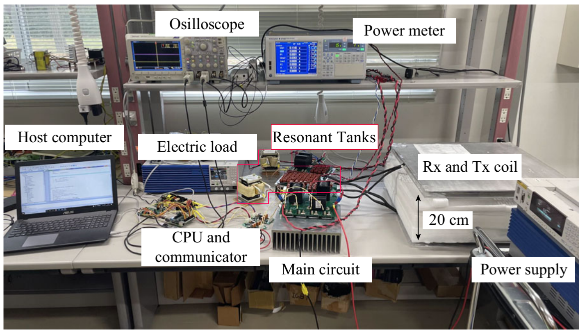

Fig. 12. Exterior appearance of the prototype.

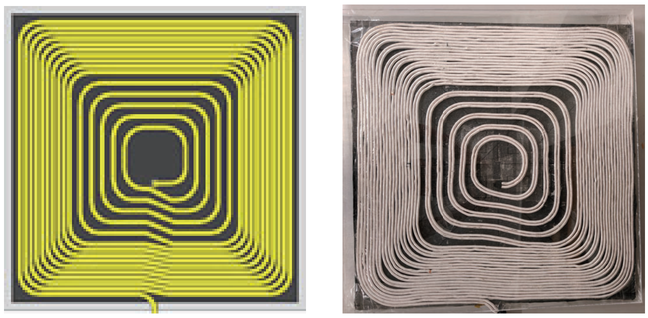

(a) (b)

Fig. 13. Rectangular Tx / Rx coil: (a) design graphics, and (b) actual appearance.

of the constraint in the facility specification. Based on (5), the rated output power can be expressed as

$$P_o^* = R_o^* I_{omax}^2 = \frac{16}{\pi^4} R_o^* \omega_r^6 M^2 C_{p1}^2 C_{p2}^2 V_{in}^2. \tag{12}$$

In addition, the voltage conversion ratio ζ is given by

$$\zeta = \frac{V_o}{V_{in}} = \frac{4}{\pi^2} R_o \omega_r^3 M C_{p1} C_{p2}. \tag{13}$$

The nominal gap length between Tx and Rx coils is set $20\,\mathrm{cm}$ ($M \simeq 27\,\mathrm{uH}$) with consideration for the actual distance between the body of EVs and ground. Then the coupling coefficient k and load ratio λ are defined as

$$k = \frac{M}{\sqrt{L_1 L_2}} \simeq 0.22$$
$$\lambda = R_o / R_o^*. \tag{14}$$

Substituting the ZPA frequency $f_r = 83\,\mathrm{kHz}$, C_{p1} and C_{p2} are approximately determined from (12) as

$$C_{p1} = C_{p2} \simeq 163\,\mathrm{nF}. \tag{15}$$

Besides, due to the impedance condition (3), the rest of main circuit parameters can also be calculated as

$$L_{s1} = L_{s2} = \frac{1}{4\pi^2 f_r^2 C_{p1}} \simeq 22.5\,\mu\mathrm{H}$$
$$C_{s1} = C_{s2} = \frac{C_{p1}}{4\pi^2 f_r^2 L_1 C_{p1} - 1} \simeq 35.8\,\mathrm{nF}. \tag{16}$$

The power controller is implemented by combination of a FPGA (Intel Cyclone 10 LP, $200\,\mathrm{MHz}$) and a floating-point processor micro computer unit (ST-MCUF407, $168\,\mathrm{MHz}$ with DSP), as illustrated in Fig. 14.

Authorized licensed use limited to: National Chung Hsing Univ.. Downloaded on August 18,2023 at 12:15:43 UTC from IEEE Xplore. Restrictions apply.
© 2023 IEEE. Personal use is permitted, but republication/redistribution requires IEEE permission. See https://www.ieee.org/publications/rights/index.html for more information.

This article has been accepted for publication in IEEE Transactions on Transportation Electrification. This is the author's version which has not been fully edited and content may change prior to final publication. Citation information: DOI 10.1109/TTE.2023.3305057

TABLE II
EXPERIMENTAL CIRCUIT PARAMETERS AND SPECIFICATIONS

Parameter	Symbol	Value
Rated dc input voltage	V_{in}	250V
Power rating	P_o^*	5.0kW
Operating frequency	f_s	81-90 kHz
ZPA frequency	f_r	83 kHz
Voltage dividing capacitors	C_{d1}/C_{d2}	200 μF
Parallel capacitors	C_{p1}/C_{p2}	165 nF
Series capacitors in Tx side	C_{s1}	37.8 nF
Series capacitors in Rx side	C_{s2}	36.7 nF
Series inductors	L_{s1}/L_{s1}	22.5 μH
Output capacitor	C_o	200 μF
Gap length of coils	l	20 cm
Coupling coefficient	k	0.22

TABLE III
TX AND RX COIL SPECIFICATIONS

Index	size and values
Coil size	500mm × 500mm
Turns	15 : 15
Self inductance L_1/L_2	125μH/125μH
Litz wire diameter	0.1mm
Bundle / twist	1300 / 2
Magnetic material	VHF ferrite absorber tile
Magnet plate size	520mm × 520mm
Insulator material	plastic
Shield size	550mm × 550mm × 5mm

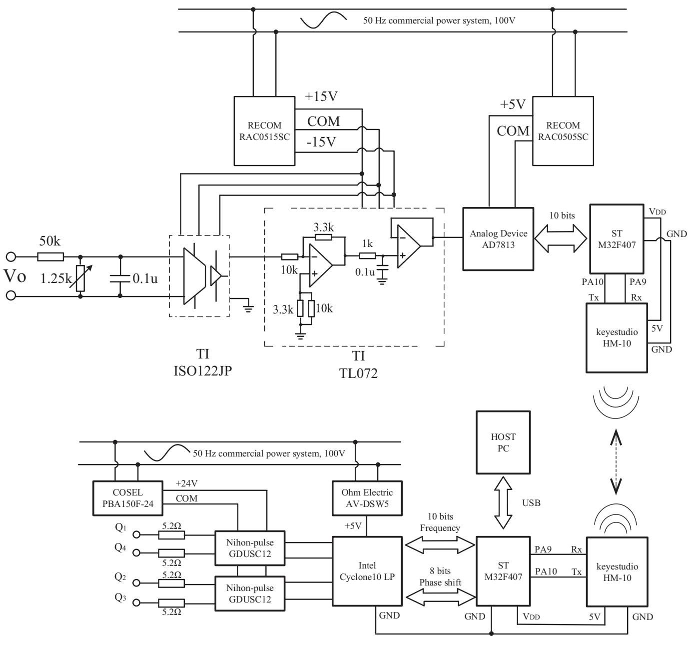

Fig. 14. Schematic diagram of signal processing and controller with Tx and Rx wireless communicator.

C. Experimental Results

The observed voltage and current waveforms of HFTL-INV are displayed in Figs. 15 (a) and (b) for CC mode. It should be remarked here that the input voltage V_{in} is reduced from the nominal one in order to avoid the over-voltage in Q_2 and Q_3 due to H-SW under the light load condition as revealed in TABLE I. All the switches Q_1-Q_4 are commutated by semi-ZVS in Fig. 15 (a) due to the pulse modulation M① as the first step of algorithm. In Fig. 15 (b), ZVS can achieve in the fixed-

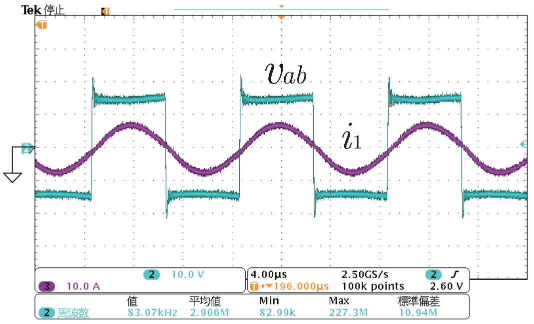

(a)

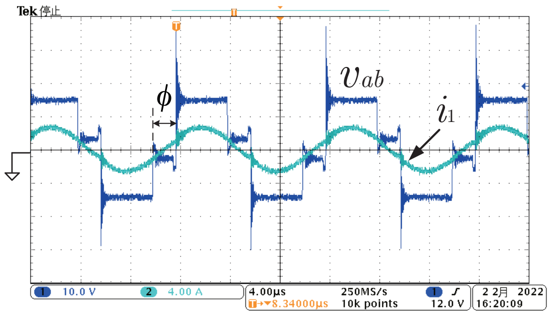

(b)

Fig. 15. Observed waveforms of HFTL-INV for CC modes: (a) $\lambda = 100\%$, (b) $\lambda = 25\%$ and $\phi = 50\,°$ (V_{in} = 30V, f_s = 83kHz).

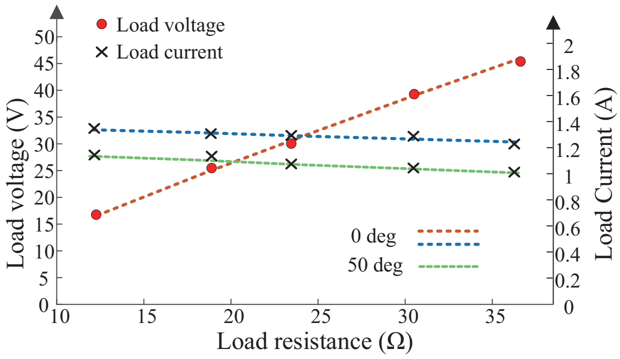

Fig. 16. Load voltage and current curves in CC mode.

phase Q_1 and Q_4 while the H-SW appears in the controlled phase Q_2 and Q_3 due to PS-PWM at $\phi = 50°$ in the pulse modulation M②. It should be remarked that ZPA maintains in the CC mode between v_{ab} and i_1 regardless of load conditions due to the effect of D-LCC. The load-independent steady-state characteristics are presented in Fig. 16 over the wide range of load variations. The load current is theoretically calculated from (1), (2), and (4) as

$$I_o = \left|\frac{\dot{Z}_4}{\dot{Z}_2\dot{Z}_6}\right| V_{ac} = 0.104 \cdot \frac{\sqrt{2}V_{in}}{\pi}\sqrt{\frac{8}{\pi^2}} \simeq 1.27\text{A}.$$
$$I_{o,50°} = \frac{(1+\cos 50°)}{2} I_o \simeq 1.04\text{A}. \tag{17}$$

It can confirmed from Fig. 16 that the load current I_o and $I_{o,\phi}$ keep almost same values as (17). Thus, the load independence of D-LCC resonant tank is actually verified with a high power factor in the HFTL-INV.

Authorized licensed use limited to: National Chung Hsing Univ.. Downloaded on August 18,2023 at 12:15:43 UTC from IEEE Xplore. Restrictions apply.
© 2023 IEEE. Personal use is permitted, but republication/redistribution requires IEEE permission. See https://www.ieee.org/publications/rights/index.html for more information.

This article has been accepted for publication in IEEE Transactions on Transportation Electrification. This is the author's version which has not been fully edited and content may change prior to final publication. Citation information: DOI 10.1109/TTE.2023.3305057

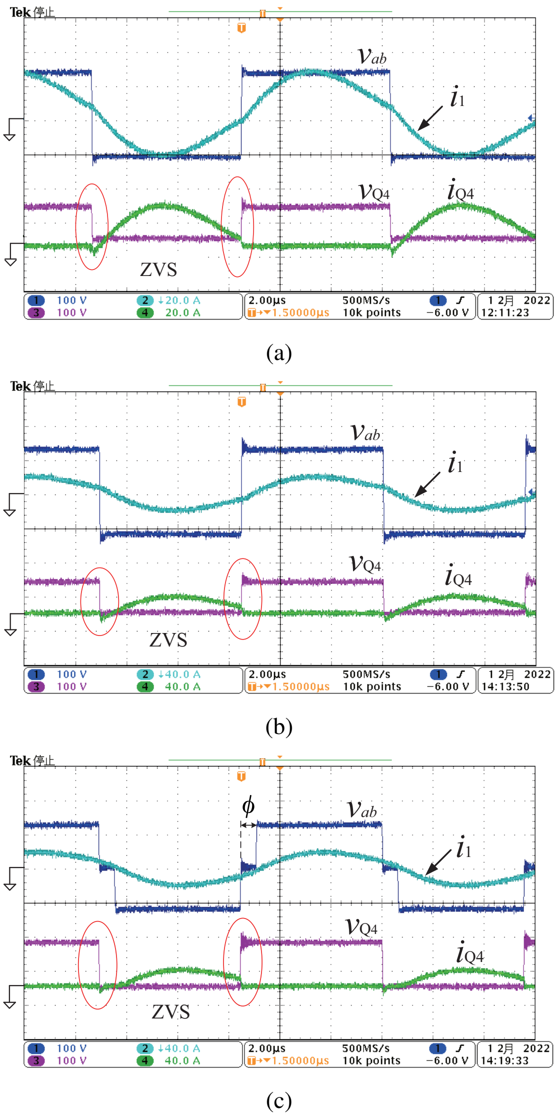

Fig. 17. Observed waveforms of HFTL-INV in CV mode: (a)$\lambda = 25\%$, f_s = 85kHz, ϕ = 0deg, (b) $\lambda = 25\%$, f_s = 90kHz, ϕ = 0deg, (c)$\lambda = 25\%$, f_s = 90kHz, ϕ = 20deg. v_{ab}: 100V/div, v_{Q4}: 100V/div, i_1: 40A/div, i_{Q4}: 40A/div.

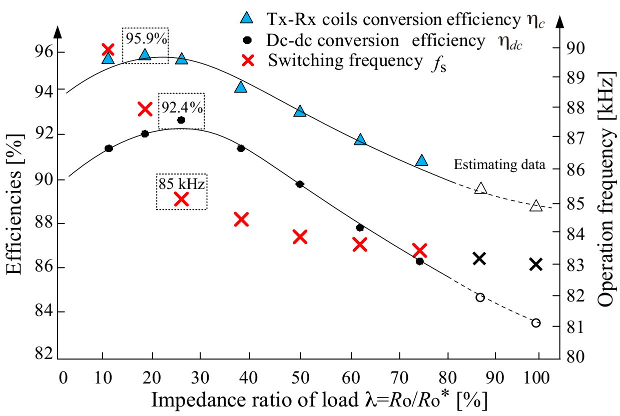

Fig. 18. Actual efficiency curves of the prototype by PFM in M③.

The observed waveforms for CV mode are provided in Fig. 17. The two-level voltage v_{ab} and the current i_1 are regulated in phase for the variations of λ from 25 % to 100 % by PFM1 for tracking maxim power points, which leads to high power factor and ZVS in Q_1-Q_4. The fixed-phase switch Q_1 (or Q_4) always achieves ZVS at the turn-on transition in Figs. 17(a)-(c) by combination of PFM and PS-PWM with the aids of lagging currents, whereas the turn-off transitions induce the relatively high dv/dt due to increase of ϕ. Accordingly, high power factor can attain with respect to fundamental components in the HFTL-INV by the load-independent and -adaptable characteristics.

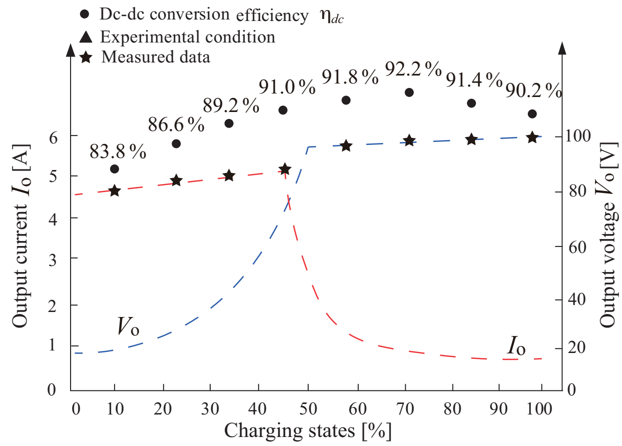

Fig. 19. Actual efficiencies in the CC and CV charging pattern.

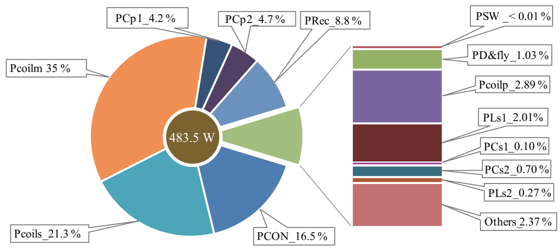

Fig. 20. Power loss breakdown for typical situations at $\lambda = 75\,\%$, $\phi = 0°$ and $f_s = 83.5\,$kHz. P_{con}: Conduction power loss, $P_{D\&fly}$ in clamping diodes and flying capacitor, P_{coilp} in Tx coils, P_{coils} in Rx coils, P_{coilm} in magnetizing inductance, P_{Ls1} in Tx series inductor, P_{Cp1} in Tx parallel capacitor, P_{Cs1} in Tx series capacitor, P_{Cs2} in Rx series capacitor, P_{Ls2} in Rx series inductor, P_{Cp2} in Rx parallel capacitor, P_{Cs2} in Rx series capacitor, and P_{PRec} in Rectifier.

The actual efficiencies including the dc-dc conversion efficiency η_{dc} are displayed in Fig. 18. The load ratio λ is constrained less than 80 % in experiment in order not to exceed the voltage rating of series and parallel capacitors in the Rx-side LCC network. The maximum dc-dc efficiency achieves 92.4 % at $P_o = 2.0\,$kW with $f_s = 85\,$kHz for $\lambda = 25\,\%$. The peak efficiency in the HFTL-INV state is 95 % at $\lambda = 20\,\%$. The coil efficiency η_c has the same trend as η_{dc}, which implies that the Tx/Rx coil cause the main power loss in the prototype.

Fig. 19 shows the actual efficiencies in a CC/CV charging process where the current and voltage commands are set as 5 A and 100 V respectively. The load current and voltage are controlled in accordance with the output modes. The efficiency achieves 83.8 %–92.2 % in the whole process.

The power loss breakdowns are revealed in Fig. 20 with

Authorized licensed use limited to: National Chung Hsing Univ.. Downloaded on August 18,2023 at 12:15:43 UTC from IEEE Xplore. Restrictions apply.
© 2023 IEEE. Personal use is permitted, but republication/redistribution requires IEEE permission. See https://www.ieee.org/publications/rights/index.html for more information.

This article has been accepted for publication in IEEE Transactions on Transportation Electrification. This is the author's version which has not been fully edited and content may change prior to final publication. Citation information: DOI 10.1109/TTE.2023.3305057

respect to the load ratios. Each power losses are based on the measurement and calculation with the parameters of power devices and components that are adopted in the prototype. The power losses in the Tx coils are outstanding especially in the heavy load. The power losses of Tx and Rx coils are reduced toward the light load. The switching losses in Q_1-Q_4 keep low values due to the effect the proposed pulse modulation as well as the aids of SiC-MOSFET. When the PS angle is set at $50°$ in PS-PWM (M②), hard switching appears in the inner switches Q_2 and Q_3. However, it still keeps a very low profile ($0.35\,\%$) since the driving-point impedance remains as inductive and ZVS can attain partly.

V. Conclusion

A ZPA load-independent and -adaptable D-LCC IPT has been proposed with high efficiency power conversion. The output voltage or current can be constant and load-independent if the network satisfies the ZPA load independent condition and be operated at the designed ZPA frequency. The output is only relevant to the shunt components in the multi-resonant tanks, thus the high-order network can be designed simply by considering the even-order impedances.

An actual system model featuring D-LCC and HFTL-INV has been built for verification of feasibility. With a new hybrid PFM / PS-PWM control strategy based on the proposed theory and impedance conditions, full-range CC/CV mode can be achieved with ZVS commutations in the HFTL-INV. A **5 kW** downscaled prototype with high-current printed circuit board, SiC MOSFETs and high capacity rectangular D-shape coils are adopted for performance investigations. The high efficiency over $95.9\,\%$ achieves in the HFTL-INV, the maximum dc-dc conversion efficiency is recorded by $92.4\,\%$ at $\lambda = 25\,\%$ condition at the gap length $g = 20\,\mathrm{cm}$.

Appendix

Equivalent Circuits of Tx and Rx Coils

The Tx and Rx coils can be modeled by HF transformer with the lumped parameter arrangements when the operating frequency is less than several hundred kHz. Figs. 21 (a)-(d) illustrate the basic and extended equivalent circuits of the Tx and Rx coils. Based on the T-type circuit model with $M = k\sqrt{L_1 L_2}$ in Fig. 21 (a), the HF transformer model with the leakage and magnetizing inductances is drawn in Fig. 21 (b). In addition the Rx-side leakage inductance l_2 can be referred to the Tx side as Fig. 21 (c). As a result, the leakage and magnetizing inductances can be expressed uniquely by L_r and L_m in Fig. 21 (d), where the winding turns ratio a' of ideal transformer (I.T.) should be defined as

$$a' = \frac{M}{L_2} = k\sqrt{\frac{L_1}{L_2}}. \tag{18}$$

Note here that a's is not identical with the actual windings ratio $a = w_1/w_2$.

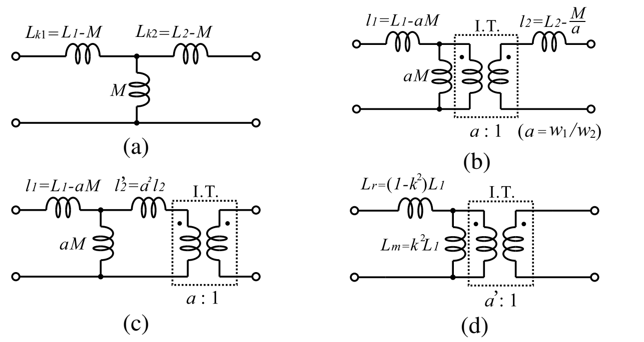

Fig. 21. Derivation of equivalent circuits for Tx and Rx coils: (a) T-type equivalent circuit, (b) HF transformer model, (c) T-type transformer model, and (d) L-type HF transformer model.

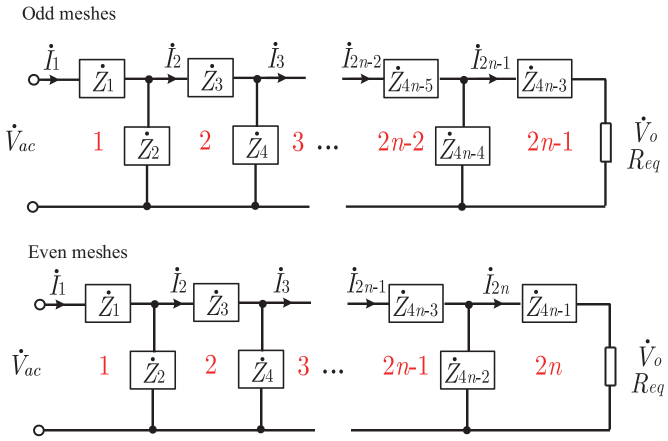

Fig. 22. Universal models for high order networks.

Load Independence of Resonant Tanks

The ZPA load-independent networks are characterized by the impedance condition that every mesh circuit can oscillate separately at the same natural frequency. The impedance conditions can be extended into the higher-order resonant tanks in IPT systems.

Most of the resonant converters can be expressed by combination of mesh circuits as depicted in Fig. 22. The relevant information of the typical resonant tanks is summarized in TABLE IV. Notice here that all of the meshes oscillate at the same frequency, whereby the impedances of odd-mesh networks satisfy the conditions as

$$\begin{cases} \dot{Z}_1 + \dot{Z}_2 = \dot{Z}_2 + \dot{Z}_3 + \dot{Z}_4 = \\ \ldots = \dot{Z}_{4n-6} + \dot{Z}_{4n-5} + \dot{Z}_{4n-4} = \\ \dot{Z}_{4n-4} + \dot{Z}_{4n-3} = 0 \end{cases} \tag{19}$$

, and those of even-mesh networks satisfy the conditions as

$$\begin{cases} \dot{Z}_1 + \dot{Z}_2 = \dot{Z}_2 + \dot{Z}_3 + \dot{Z}_4 = \\ \ldots = \dot{Z}_{4n-4} + \dot{Z}_{4n-3} + \dot{Z}_{4n-2} \\ \dot{Z}_{4n-2} + \dot{Z}_{4n-1} = 0. \end{cases} \tag{20}$$

Authorized licensed use limited to: National Chung Hsing Univ.. Downloaded on August 18,2023 at 12:15:43 UTC from IEEE Xplore. Restrictions apply.
© 2023 IEEE. Personal use is permitted, but republication/redistribution requires IEEE permission. See https://www.ieee.org/publications/rights/index.html for more information.

This article has been accepted for publication in IEEE Transactions on Transportation Electrification. This is the author's version which has not been fully edited and content may change prior to final publication. Citation information: DOI 10.1109/TTE.2023.3305057

TABLE IV
RESONANT TANKS IN WPT SYSTEM

Networks	Meshes	Specifications
S-S	2	$\dot{Z}_1+\dot{Z}_2=\dot{Z}_2+\dot{Z}_3=0$
S-P	3	$\dot{Z}_1+\dot{Z}_2=\dot{Z}_2+\dot{Z}_3+\dot{Z}_4=\dot{Z}_5=0$
P-S	3	$\dot{Z}_1=\dot{Z}_2+\dot{Z}_3+\dot{Z}_4=\dot{Z}_4+\dot{Z}_5=0$
P-P	4	$\dot{Z}_1=\dot{Z}_2+\dot{Z}_3+\dot{Z}_4=...=\dot{Z}_7=0$
LCC-S	3	$\dot{Z}_1+\dot{Z}_2=\dot{Z}_2+\dot{Z}_3+\dot{Z}_4=\dot{Z}_4+\dot{Z}_5=0$
D-LCC	4	$\dot{Z}_1+\dot{Z}_2=...=\dot{Z}_6+\dot{Z}_7=0.$

The Kirchhoff's Voltage Law (KVL) equations are written for the odd-mesh networks as

$$\begin{cases}\dot{V}_{ac}=\dot{Z}_1\dot{I}_1+\dot{Z}_2(\dot{I}_1-\dot{I}_2)\\ \dot{Z}_2(\dot{I}_1-\dot{I}_2)=\dot{Z}_3\dot{I}_2+\dot{Z}_4(\dot{I}_2-\dot{I}_3)\\ \dot{Z}_4(\dot{I}_2-\dot{I}_3)=\dot{Z}_5\dot{I}_3+\dot{Z}_6(\dot{I}_3-\dot{I}_4)\\ \dot{Z}_6(\dot{I}_3-\dot{I}_4)=\dot{Z}_7\dot{I}_4+\dot{Z}_8(\dot{I}_4-\dot{I}_5)\quad ...\\ \dot{Z}_{4n-6}(\dot{I}_{2n-3}-\dot{I}_{2n-2})=\dot{Z}_{4n-5}\dot{I}_{2n-2}\\ \qquad\qquad +\dot{Z}_{4n-4}(\dot{I}_{2n-2}-\dot{I}_{2n-1})\\ \dot{Z}_{4n-4}(\dot{I}_{2n-2}-\dot{I}_{2n-1})=\dot{Z}_{4n-3}\dot{I}_{2n-1}+R_{eq}\dot{I}_{2n-1}\end{cases}\tag{21}$$

and for the even-mesh networks

$$\begin{cases}\dot{V}_{ac}=\dot{Z}_1\dot{I}_1+\dot{Z}_2(\dot{I}_1-\dot{I}_2)\\ \dot{Z}_2(\dot{I}_1-\dot{I}_2)=\dot{Z}_3\dot{I}_2+\dot{Z}_4(\dot{I}_2-\dot{I}_3)\\ \dot{Z}_4(\dot{I}_2-\dot{I}_3)=\dot{Z}_5\dot{I}_3+\dot{Z}_6(\dot{I}_3-\dot{I}_4)\\ \dot{Z}_6(\dot{I}_3-\dot{I}_4)=\dot{Z}_7\dot{I}_4+\dot{Z}_8(\dot{I}_4-\dot{I}_5)\quad ...\\ \dot{Z}_{4n-4}(\dot{I}_{2n-2}-\dot{I}_{2n-1})=\dot{Z}_{4n-3}\dot{I}_{2n-1}\\ \qquad\qquad +\dot{Z}_{4n-2}(\dot{I}_{2n-1}-\dot{I}_{2n})\\ \dot{Z}_{4n-2}(\dot{I}_{2n-1}-\dot{I}_{2n})=\dot{Z}_{4n-1}\dot{I}_{2n}+R_{eq}\dot{I}_{2n}.\end{cases}\tag{22}$$

By using (19), the KVL equations in (21) can be simplified as

$$\begin{cases}\dot{V}_{ac}=-\dot{Z}_2\dot{I}_2\\ \dot{Z}_2\dot{I}_1=-\dot{Z}_4\dot{I}_3\\ \dot{Z}_4\dot{I}_2=-\dot{Z}_6\dot{I}_4\\ \dot{Z}_6\dot{I}_3=-\dot{Z}_8\dot{I}_5\quad ...\\ \dot{Z}_{4n-6}\dot{I}_{2n-3}=-\dot{Z}_{4n-4}\dot{I}_{2n-1}\\ \dot{Z}_{4n-4}\dot{I}_{2n-2}=R_{eq}\dot{I}_{2n-1}\end{cases}\tag{23}$$

and in (20) as

$$\begin{cases}\dot{V}_{ac}=-\dot{Z}_2\dot{I}_2\\ \dot{Z}_2\dot{I}_1=-\dot{Z}_4\dot{I}_3\\ \dot{Z}_4\dot{I}_2=-\dot{Z}_6\dot{I}_4\\ \dot{Z}_6\dot{I}_3=-\dot{Z}_8\dot{I}_5\quad ...\\ \dot{Z}_{4n-4}\dot{I}_{2n-2}=-\dot{Z}_{4n-2}\dot{I}_{2n}.\end{cases}\tag{24}$$

The output voltage and current of the multi-resonant tanks in Fig. 22 can be defined mathematically as follows.

[Odd-mesh networks with voltage source input]: When the odd-mesh networks are connected with a voltage source, the $1^{st},3^{rd},...,(2n-1)^{nd}$ equations of (23) are applicable, thereby the load current and voltage can be derived as

$$\begin{cases}\dot{I}_{2n-1}=(-1)^{n-1}\dfrac{\prod\limits_{m=1}^{n-1}\dot{Z}_{4m}}{R_{eq}\prod\limits_{h=1}^{n-1}\dot{Z}_{4h-2}}\dot{V}_{ac}(n=2,3,4...)\\ \dot{V}_o=R_{eq}\dot{I}_{2n-1}=-1)^{n-1}\dfrac{\prod\limits_{m=1}^{n-1}\dot{Z}_{4m}}{\prod\limits_{h=1}^{n-1}\dot{Z}_{4h-2}}\dot{V}_{ac}(n=2,3,4...).\end{cases}\tag{25}$$

[Even-mesh networks with voltage source input]: When the even-mesh networks are driven by a voltage source, the 1^{st}, 3^{rd},..., $(2n-1)^{nd}$ equation of (24) are effective. Then, the load current and voltage are given by

$$\begin{cases}\dot{I}_{2n}=(-1)^{n}\dfrac{\prod\limits_{m=1}^{n-1}\dot{Z}_{4m}}{\prod\limits_{h=1}^{n}\dot{Z}_{4h-2}}\dot{V}_{ac}(n=2,3,4...)\\ \dot{V}_o=R_{eq}\dot{I}_{2n}=(-1)^{n}\dfrac{R_{eq}\prod\limits_{m=1}^{n-1}\dot{Z}_{4m}}{\prod\limits_{h=1}^{n}\dot{Z}_{4h-2}}\dot{V}_{ac}(n=2,3,4...).\end{cases}\tag{26}$$

[Odd-mesh networks with current source input]: When the odd-mesh networks are driven by a current source, the 2^{nd}, 4^{th},...,$(2n-2)^{nd}$ equations in (23) are available. Thus, the load current and voltage can be expressed as

$$\begin{cases}\dot{I}_{2n-1}=(-1)^{n}\dfrac{\prod\limits_{m=1}^{n-1}\dot{Z}_{4m-2}}{\prod\limits_{h=1}^{n-1}\dot{Z}_{4h}}\dot{I}_1(n=2,3,4...)\\ \dot{V}_o=R_{eq}\dot{I}_{2n-1}=(-1)^{n}\dfrac{R_{eq}\prod\limits_{m=1}^{n-1}\dot{Z}_{4m-2}}{\prod\limits_{h=1}^{n-1}\dot{Z}_{4h}}\dot{I}_1(n=2,3,4...).\end{cases}\tag{27}$$

[Even-mesh networks with current source input]: When the even-mesh networks are connected with a current source, the 2^{nd}, 4^{th},..., $2n^{nd}$ equations of (24) are utilized to produce the load current and voltage as

$$\begin{cases}\dot{I}_{2n}=(-1)^{n}\dfrac{\prod\limits_{m=1}^{n}\dot{Z}_{4m-2}}{R_{eq}\prod\limits_{h=1}^{n-1}\dot{Z}_{4h}}\dot{I}_1(n=2,3,4...)\\ \dot{V}_o=R_{eq}\dot{I}_{2n}=(-1)^{n}\dfrac{\prod\limits_{m=1}^{n}\dot{Z}_{4m-2}}{\prod\limits_{h=1}^{n-1}\dot{Z}_{4h}}\dot{I}_1(n=2,3,4...).\end{cases}\tag{28}$$

The characteristics of resonant tanks are summarized in TABLE V. Thus, the ZPA load-independent resonant tanks have distinctive features at the designed frequency where (19) or (20) can be established:

Authorized licensed use limited to: National Chung Hsing Univ.. Downloaded on August 18,2023 at 12:15:43 UTC from IEEE Xplore. Restrictions apply.
© 2023 IEEE. Personal use is permitted, but republication/redistribution requires IEEE permission. See https://www.ieee.org/publications/rights/index.html for more information.

This article has been accepted for publication in IEEE Transactions on Transportation Electrification. This is the author's version which has not been fully edited and content may change prior to final publication. Citation information: DOI 10.1109/TTE.2023.3305057

TABLE V
LOAD INDEPENDENT CHARACTERISTICS OF RESONANT TANKS

n	circuits	voltage source	output	current source	output
$n=1, odd$	Series oscillator	$\dot{V}_o = \dot{V}_{ac}$	CV	$\dot{V}_o = R_{eq}\dot{I}_1$	CC
$n=1, even$	S-S($\dot{Z}_2 \neq 0$)	$\dot{V}_o = -R_{eq}\frac{1}{\dot{Z}_2}\dot{V}_{ac}$	CC	$\dot{V}_o = \dot{Z}_2\dot{I}_1$	CV
$n>1, odd$	LCC-S (n=2)	$\dot{V}_o = R_{eq}\dot{I}_{2n-1} = (-1)^{n-1}\frac{\prod_{m=1}^{n-1}\dot{Z}_{4m}}{\prod_{h=1}^{n-1}\dot{Z}_{4h-2}}\dot{V}_{ac}$	CV	$\dot{V}_o = R_{eq}\dot{I}_{2n-1} = (-1)^{n}\frac{R_{eq}\prod_{m=1}^{n-1}\dot{Z}_{4m-2}}{\prod_{h=1}^{n-1}\dot{Z}_{4h}}\dot{I}_1$	CC
$n>1, even$	$D-LCC(n=2)$	$\dot{V}_o = R_{eq}\dot{I}_{2n} = (-1)^{n}\frac{R_{eq}\prod_{m=1}^{n-1}\dot{Z}_{4m}}{\prod_{h=1}^{n}\dot{Z}_{4h-2}}\dot{V}_{ac}$	CC	$\dot{V}_o = R_{eq}\dot{I}_{2n} = (-1)^{n}\frac{\prod_{m=1}^{n}\dot{Z}_{4m-2}}{\prod_{h=1}^{n-1}\dot{Z}_{4h}}\dot{I}_1$	CV

1) Multi-resonant tank can naturally achieve CC or CV output mode, which is dependent on the source type.
2) The output voltage and current are only relevant to all the parallel components (or even-order components, $\dot{Z}_2.\dot{Z}_4, \dot{Z}_6...$) and load resistance.

As a summary based on the equations from (25) to (28), the parallel impedances of the ZPA load-independent resonant tanks should not be zero to produce the output power as expressed by

$$\dot{Z}_2\dot{Z}_4...\dot{Z}_{4n-4} \neq 0 \quad (n = 2, 3, 4...) \tag{29}$$

and in the even networks as

$$\dot{Z}_2\dot{Z}_4...\dot{Z}_{4n-2} \neq 0 \quad (n = 2, 3, 4...). \tag{30}$$

ACKNOWLEDGMENT

The authors would like to appreciate Mr. Tian Luo for the cooperations in analysis and experiments.

REFERENCES

[1] B. Esteban, M. Sid-Ahmed and N. C. Kar, "A comparative study of power supply architectures in wireless EV charging systems," *IEEE Trans. Power Electron.*, vol. 30, no. 11, pp. 6408–6422, Nov. 2015.
[2] K. Aditya and S. S. Williamson, "A review of optimal conditions for achieving maximum power output and maximum efficiency for a series-series resonant inductive link," *IEEE Trans. Transport. Electrification*, vol. 3, no. 2, pp. 303–311, June 2017.
[3] W. Zhang and C. C. Mi, "Compensation topologies of high-power wireless power transfer systems," *IEEE Trans. Vehicular Tech.*, vol. 65, no. 6, pp. 4768–4778, June 2016.
[4] M. S. Haque, M. Mohammad and S. Choi, "Sensitivity analysis and controller design of high power LCC-LCC compensated wireless battery charging for electric ship applications," *2020 IEEE Appl. Power Electron. Conf. Expo.*, New Orleans, LA, USA, 2020, pp. 3200–3207.
[5] W. Liu, K. T. Chau, C. H. T. Lee, W. Han, X. Tian and W. H. Lam, "Full-range soft-switching pulse frequency modulated wireless power transfer," *IEEE Trans. Power Electron.*, vol. 35, no. 6, pp. 6533–6547, June 2020.
[6] T. Mishima and C.-M. Lai, "Load-adaptive resonant frequency-tuned-pulse density modulation for class-D ZVS high-frequency inverter-based inductive wireless power transfer," *IEEE Jour. Emerg. Sel. Top. Ind. Electron.*.
[7] F. Lu, H. Zhang, H. Hofmann, W. Su, and C.C Mi, "A dual-coupled LCC-compensated IPT system with a compact magnetic coupler," *IEEE Trans. Power Electron.*, vol.33, no.7, pp.6391-6402, Jul. 2018.
[8] W. Liu, K. T. Chau, C. H. T. Lee, X. Tian and C. Jiang, "Hybrid Frequency Pacing for High-Order Transformed Wireless Power Transfer," *IEEE Trans. Power Electron.,* vol. 36, no. 1, pp. 1157-1170, Jan. 2021.
[9] J. Lu, G. Zhu, D. Lin, S.-C. Wong, and J. Jiang, "Load-independent voltage and current transfer characteristics of high-order resonant network in IPT system," *IEEE J. Emerg. Sel. Topics Power Electron.*, vol.7, no.1, pp.422-436, Mar. 2019.
[10] J. Lu, G. Zhu, D. Lin, Y. Zhang, J. Jiang and C. C. Mi, "Unified load-independent ZPA analysis and design in CC and CV modes of higher order resonant circuits for WPT systems," *IEEE Trans. Transport. Electrif.*, vol. 5, no. 4, pp. 977-987, Dec. 2019.
[11] V.-B. Vu, D.-H. Tran, and W. Choi, "Implementation of the constant current and constant voltage charge of inductive power transfer systems with the double-sided LCC compensation topology for electric vehicle battery charge applications, "*IEEE Trans. Power Electron.*, vol.33, no.9, pp.7398-7410, Sep. 2018.
[12] B. Cheng and L. He, "High-order network based general modeling method for improved transfer performance of the WPT system, *IEEE Trans. Power Electron.,* vol. 36, no. 11, pp. 12375-12388, Nov. 2021.
[13] J. Lu, G. Zhu, H. Wang, F. Lu, J. Jiang, and C.C. Mi, "Sensitivity analysis of inductive power transfer systems with voltage-fed compensation topologies," *IEEE Trans. Vehicular Tech.*, vol.68, no.5, pp.4502-4513, May 2019.
[14] J. Li, X. Zang, and X. Tong, "Research and design of misalignment-tolerant LCC-LCC compensated IPT system with constant-current and constant-voltage output," *IEEE Trans. Power Electron.*, vol.38, no.1, pp.1301-1313, Jan. 2023.
[15] Z. Luo, Y. Zhao, M. Xiong, X. Wei, and H. Dai, "A self-tuning LCC/LCC system based on switch-controlled capacitors for constant power wireless electric vehicle charging," *IEEE Trans. Ind. Electron.*, vol.70, no.1, pp.709-720, Jan. 2023.
[16] H. Li, J. Xu, F. Gao, Y. Zhang, X. Yang, and H. Tang, "Duty cycle control strategy for dual-side LCC resonant converter," *IEEE Trans. Transp. Electrific.*, vol.8, no.2, pp.1944-1955, Jun. 2022.
[17] T. Mishima and E. Morita, "High-frequency bridgeless rectifier based ZVS Multiresonant converter for inductive power Transfer Featuring High-Voltage GaN-HFET," *IEEE Trans. Ind. Electron,* vol.64, no.11, pp.9155-9164, Nov. 2017.
[18] Y. Chen, H. Zhang, C.-S. Shin, C.-H. Jo, S.J. Park, and D.-H. Kim, "An efficiency optimization-based asymmetric tuning method of double-sided LCC compensated WPT system for electric vehicles," *IEEE Trans. Power Electron.*, vol.35, no.11, pp.11475-11487, Nov. 2020.
[19] M. Mohammad, etal, "Bidirectional LCC-LCC-compensated $20-\mathrm{kW}$ wireless power transfer system for medium-duty vehicle charging," *IEEE Trans. Transport. Electrif.*, vol.7, no.3, pp.1205-1218, Mar. 2021.
[20] T. Luo, T. Mishima and C. -M. Lai, "High frequency three-level inverter-based inductive wireless power transfer (IPT) system with double LCC resonance," *2021 IEEE Appl. Power Electron. Conf. and Expo. (APEC)*, Phoenix, AZ, USA, 2021, pp. 413–420.
[21] D. Fu, F. C. Lee, Y. Qiu and F. Wang, "A novel high-power-density three-level LCC resonant converter with constant-power-factor-control for charging applications," *IEEE Trans. Power Electron.*, vol. 23, no. 5, pp. 2411–2420, Sept. 2008.
[22] S. Moon, B.-C. Kim, S.-Y. Cho, C.-H. Ahn, and G.-W. Moon, "Analysis and design of a wireless power transfer system with an intermediate coil for high efficiency," *IEEE Trans. Ind. Electron.*, vol. 61, no. 11, pp. 5861-5870, Nov. 2014.
[23] M. Kasper, R. M. Burkart, G. Deboy and J. W. Kolar, "ZVS of power MOSFETs revisited," *IEEE Trans. Ind. Electron,* vol. 31, no. 12, pp. 8063-8067, Dec. 2016.

Authorized licensed use limited to: National Chung Hsing Univ.. Downloaded on August 18,2023 at 12:15:43 UTC from IEEE Xplore. Restrictions apply.
© 2023 IEEE. Personal use is permitted, but republication/redistribution requires IEEE permission. See https://www.ieee.org/publications/rights/index.html for more information.

This article has been accepted for publication in IEEE Transactions on Transportation Electrification. This is the author's version which has not been fully edited and content may change prior to final publication. Citation information: DOI 10.1109/TTE.2023.3305057

Tomokazu Mishima (S'00–M'04–SM'15) received the Ph.D. degree in electrical engineering from The University of Tokushima, Japan in 2004. Since 2010, he has been with Kobe University, Hyogo, Japan as an associate professor, and engages in the researches and developments of power electronics circuits and systems. Dr. Mishima has been appointed to the Center for Advanced Medical Engineering Research and Development (CAMED), Kobe University since 2020, where he engages in research and development of wireless power transfer systems for implantable devices. His research interests include soft-switching dc–dc converters, resonant converters, and high frequency inverters for industrial, automotive, biomedical, renewable and sustainable energy applications.

Dr. Mishima is the recipients of 2022 IEEE Transactions on Power Electronics Second Place Prize Paper Award, and the best paper award in the 2009 IEEE International Conference on Power Electronics and Drive Systems (PEDS), and the best paper presentation award in 2012 Annual Conference of the IEEE Industrial Electronics Society (IECON). He serves as the associate editor of IEEE Transactions on Power Electronics, and the chairperson of the semiconductor power converter sector in IEEJ (The Institute of Electrical Engineering of Japan) Transactions on Industry Applications.

Dr. Mishima is a senior member of IEEJ, and members of IEICE (The Institute of Electronics, Information and Communication Engineers) and JIPE (the Japan Institute of Power Electronics).

Ching-Ming Lai (S'06–M'10–SM'17) received the Ph.D. degree in electrical engineering from National Tsing Hua University (NTHU), Hsinchu, Taiwan, in 2010. Since 2019, Dr. Lai is an Associate Professor with the Department of Electrical Engineering in National Chung Hsing University (NCHU), Taiwan, where he is also the director of intelligent electric vehicle green energy center (i-Center).

Dr. Lai received the best paper award at the 2013 IEEE International Conference on Power Electronics and Drive Systems. He was the recipient of the 2008 Young Author's Award for Practical Application from the Society of Instrument and Control Engineers (SICE), Japan. He received the Best Paper Award of three papers from TaiPEA in 2007–2010, one Excellent Paper Award at National Symposium on Taiwan Electrical Power Engineering, 2009, and two Excellent Paper Awards at the annual conference of SAE-Taipei, 2016 and 2017. He serviced as an Associate Editor for IEEE Transactions on Industrial Electronics, from May 2018 to June 2020, IEICE Electronics Express, from June 2018 to May 2021, and IEEE Transactions on Circuit and Systems–II from October 2018 to December 2019. He has been serving as an Editor for the IEEE Transactions on Vehicular Technology, since 2017, and an Associate Editor for IEEE ACCESS, since 2021.

Dr. Lai is a Fellow of the Institution of Engineering and Technology (IET), a Fellow of the Australian Institute of Energy (AIE), and a Life Member of the Taiwan Power Electronics Association (TaiPEA).

Authorized licensed use limited to: National Chung Hsing Univ.. Downloaded on August 18,2023 at 12:15:43 UTC from IEEE Xplore. Restrictions apply.
© 2023 IEEE. Personal use is permitted, but republication/redistribution requires IEEE permission. See https://www.ieee.org/publications/rights/index.html for more information.